

# Cyclic 2.5D Perceptual Loss for Cross-Modal 3D Image Synthesis: T1 MRI to Tau-PET

Symac Kim<sup>a</sup>, Junho Moon<sup>b</sup>, Haejun Chung<sup>a,b,c,†</sup>, Ikbeom Jang<sup>d,†</sup>, for the Alzheimer’s  
Disease Neuroimaging Initiative\*

<sup>a</sup>*Department of Artificial Intelligence, Hanyang University, Seoul 04763, South Korea*

<sup>b</sup>*Department of Artificial Intelligence Semiconductor Engineering, Hanyang University, Seoul 04763, South Korea*

<sup>c</sup>*Department of Electronic Engineering, Hanyang University, Seoul 04763, South Korea*

<sup>d</sup>*Division of Computer Engineering, Hankuk University of Foreign Studies, Yongin-si 17035, South Korea*

---

## Abstract

Alzheimer’s Disease (AD) is the most common form of dementia, characterised by cognitive decline and biomarkers such as tau-proteins. Tau-positron emission tomography (tau-PET), which employs a radiotracer to selectively bind, detect, and visualise tau protein aggregates within the brain, is valuable for early AD diagnosis but is less accessible due to high costs, limited availability, and its invasive nature. Image synthesis with neural networks enables the generation of tau-PET images from more accessible T1-weighted magnetic resonance imaging (MRI) images. To ensure high-quality image synthesis, we propose a cyclic 2.5D perceptual loss combined with mean squared error and structural similarity index measure (SSIM) losses. The cyclic 2.5D perceptual loss sequentially calculates the axial 2D average perceptual loss for a specified number of epochs, followed by the coronal and sagittal planes for the same number of epochs. This sequence is cyclically performed, with intervals reducing as the cycles repeat. We conduct supervised synthesis of tau-PET images from T1w MRI images using 516 paired T1w MRI and tau-PET 3D images from the ADNI database. For the collected data, we perform preprocessing, including intensity standardisation for tau-PET images from each manufacturer. The proposed loss, applied to generative 3D U-Net and its variants, outperformed those with 2.5D and 3D perceptual losses in SSIM and peak signal-to-noise ratio (PSNR). In addition, including the cyclic 2.5D perceptual loss to the original losses of GAN-based image synthesis models such as CycleGAN and Pix2Pix improves SSIM and PSNR by at least 2% and 3%. Furthermore, by-manufacturer PET standardisation helps the models in synthesising high-quality images than min-max PET normalisation.

*Keywords:* Image-to-Image Translation, Image Synthesis, Brain Tau-PET, Perceptual Loss

---

<sup>†</sup>Corresponding authors

*Email addresses:* [haejun@hanyang.ac.kr](mailto:haejun@hanyang.ac.kr) (Haejun Chung), [ijang@hufs.ac.kr](mailto:ijang@hufs.ac.kr) (Ikbeom Jang)

\*Data used in preparation of this article were obtained from the Alzheimer’s Disease Neuroimaging Initiative (ADNI) database ([adni.loni.usc.edu](http://adni.loni.usc.edu)). As such, the investigators within the ADNI contributed to the design and implementation of ADNI and/or provided data but did not participate in analysis or writing of this report. A complete listing of ADNI investigators can be found at: [http://adni.loni.usc.edu/wp-content/uploads/how\\_to\\_apply/ADNI\\_Acknowledgement\\_List.pdf](http://adni.loni.usc.edu/wp-content/uploads/how_to_apply/ADNI_Acknowledgement_List.pdf)

## 1. Introduction

Alzheimer’s Disease (AD) is the most prevalent form of dementia that causes cognitive impairment, including amnesic symptoms (Knopman et al., 2021). No cure for AD has been found, and diagnosis of AD occurs in the late stage for most of the patients (van der Flier et al., 2023). It is essential to diagnose AD early as early treatments lead to a better prognosis of the patient’s cognitive function (Rasmussen and Langerman, 2019).

There are two significant biomarkers that define AD: the existence of plaques consisting of beta-amyloid and neurofibrillary tangles that include tau-protein (Knopman et al., 2021; Buchhave et al., 2012). Therefore, beta-amyloid and tau-protein are considered solid indicators for monitoring or diagnosing AD. Several studies suggest that tau-protein is a better indicator than beta-amyloid for early-stage diagnosis of AD. For instance, Bucci et al. (2021) demonstrates that tau-Positron emission tomography (tau-PET) positivity predicts the decline of cognitive ability better than beta-amyloid in long-term follow-up for the AD continuum.

PET is less accessible than other imaging modalities, such as magnetic resonance imaging (MRI) and computed tomography (CT), as PET imaging is invasive, expensive, and rarely available in primary care (Guo et al., 2021); brain tau-PET is less accessible than other common imaging modalities despite the usefulness of tau-PET. This low accessibility of PET images is not limited to tau-PET but to other modes, such as beta-amyloid PET. Therefore, multiple attempts to generate those modalities from less expensive and more available modalities, such as MRI and CT, exist (Jang et al., 2023; Shin et al., 2020; Zhang et al., 2022). However, few studies attempted to generate 3D tau-PET images from 3D MRI images. Jang et al. (2023) proposed TauPETGen that synthesises realistic tau-PET images with either an MRI image with Mini Mental State Examination (MMSE) values (given by text) or text only, but it requires MMSE values as an input and dedicated to 2D images.

We retrieved 516 3D T1-weighted (T1w) MRI and 3D Tau PET pairs from subjects with either AD, Mild Cognitive Impairment (MCI), Late MCI (LMCI), and Early MCI (EMCI) from the ADNI-3 dataset. We performed preprocessing based on the procedures we suggested, including non-uniformity intensity (N3) normalisation (Sled et al., 1998), stripping skull and non-necessary tissues (also known as ‘skullstrip’), and by-manufacturer intensity standardisation for PET images.

In this study, We introduce a cyclic 2.5D perceptual loss method for 3D medical images. This method sequentially applies the axial 2D average perceptual loss for a certain number of epochs, followed by the coronal 2D average perceptual loss for the same number of epochs, and then the sagittal 2D average perceptual loss for an equivalent number of epochs. This sequence constitutes one complete cycle. As training progresses, the cycle repeats with progressively smaller numbers of epochs.

We combined the cyclic 2.5D perceptual loss that combines mean squared error (MSE) and structural similarity index measure (SSIM) loss, then applied the combined loss to a 3D U-Net-based model designed for translating T1-weighted MRI images to tau-PET images.

Our results demonstrate that the proposed loss function significantly improves both PSNR and SSIM metrics in 2D and 3D views across various experimental settings. We apply the loss to other image-to-image translation models, and the result shows that those generated higher-quality images when the combined loss is applied. Furthermore, we highlight the effectiveness of our preprocessing approach in enhancing the quality of tau-PET images generated from MRI inputs, demonstrating its potential utility in both clinical and research applications.

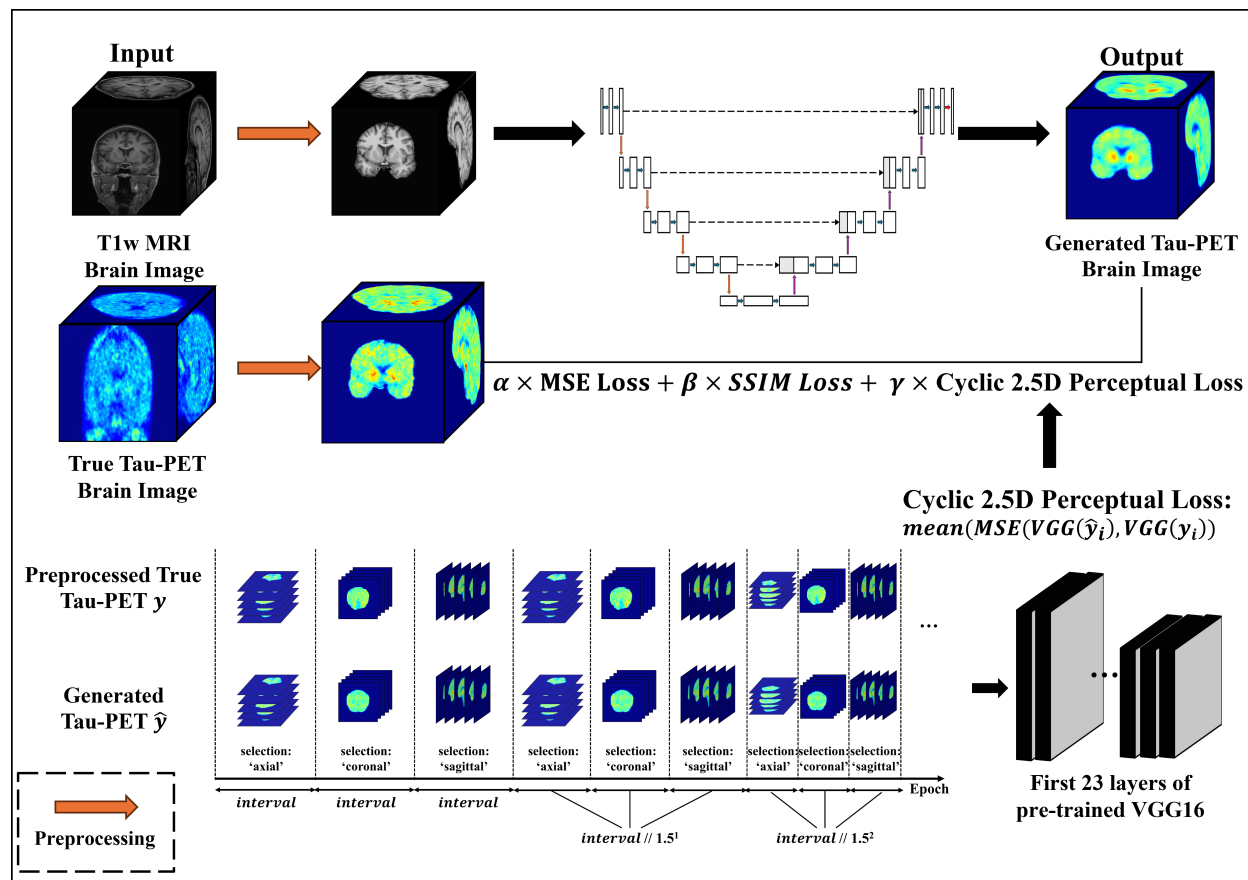


Figure 1: Overview of the image synthesis from T1w MRI brain image to tau-PET brain image. Our framework consists of preprocessing of the MRI and PET images, 3D U-Net, and combined loss of MSE loss, SSIM loss, and the proposed cyclic 2.5D perceptual loss.

## 2. Backgrounds and Related Works

### 2.1. Tau-PET

PET imaging detects pairs of high-energy photons from positron-emitting radioisotopes, allowing for high sensitivity and precise measurement of radiotracer concentrations in vivo (Vaquero and Kinahan, 2015). Depending on the desired target, different radiotracers are required. For example,  $[^{18}\text{F}]\text{FDG}$  (Fluorodeoxyglucose) is a radiotracer used for  $^{18}\text{F}\text{-FDG-PET}$  to detect, determine the stage, and monitor the medical therapy’s effect on various malignancies because glucose level increases in various malignancies and  $[^{18}\text{F}]\text{FDG}$  is a radiolabelled analogue of glucose (Delbeke et al., 2006).

Tau-PET is a form of PET imaging used to diagnose tauopathies, the neurodegenerative disorders related to the deposition of misfolded Tau proteins, such as AD and Parkinson’s Disease, using dedicated radiotracers (Leuzy et al., 2019).

First-generation radiotracers used for Tau-PET comprise  $[^{18}\text{F}]\text{THK5317}$ ,  $[^{18}\text{F}]\text{THK5351}$ ,  $[^{18}\text{F}]\text{AV-1451}$  (also known as  $[^{18}\text{F}]\text{AV-flortaucipir}$ ), and  $[^{11}\text{C}]\text{PBB3}$  (Petersen et al., 2022; Leuzy et al., 2019).  $[^{18}\text{F}]\text{AV-1451}$ , the first FDA-approved molecule amongst these, exhibits a strong and specific affinity for tau aggregates in the brain with minimal to no binding to beta-amyloid (Petersen et al., 2022; Mattay et al., 2020). It also effectively penetrates the blood-brain barrier (BBB) and demonstrates a favourable metabolic profile (Petersen et al., 2022). Although it shows insufficient affinity in non-Alzheimer’s disease cases, it is an effective tracer for AD-diagnosing tau-PET, demonstrating high sensitivity for AD samples (Petersen et al., 2022).

## 2.2. Perceptual Loss

Johnson et al. (2016) claimed that traditional per-pixel losses cannot efficiently capture perceptual differences. For instance, if an image is shifted to the right-hand side by a single pixel, per-pixel losses will significantly increase even though the original and modified images are nearly identical in human perception. Therefore, Johnson et al. (2016) suggested two perceptual losses: feature reconstruction loss and style reconstruction Loss. Feature reconstruction loss compares feature maps of a layer from a pre-trained model based on deep CNN models such as VGG (Simonyan and Zisserman, 2015), AlexNet (Krizhevsky et al., 2012), and ResNet(He et al., 2016) for the ground-truth image and the generated images by calculating average squared Euclidean distance between the maps. Style reconstruction loss is retrieved by the squared Frobenius norm of the difference of Gram matrices from both images to analyse style similarity.

Although the perceptual loss was used for style transfer and super-resolution initially (Johnson et al., 2016; Dosovitskiy and Brox, 2016), it is also applicable to other tasks such as image generation (Hou et al., 2017; Dosovitskiy and Brox, 2016) and image-to-image translation (Qu et al., 2018) in both 2D and 3D formats. In applications, feature reconstruction loss is more commonly applied as a ‘perceptual loss’, even if there is no style reconstruction loss (Liu et al., 2021); we also consider the feature construction loss as a perceptual loss in this study. The perceptual loss in 2D images is described as:

$$L_{perc}^{\phi,j}(\hat{y}, y) = \frac{1}{C_j H_j W_j} \|\phi_j(\hat{y}) - \phi_j(y)\|_2^2 \quad (1)$$

Where  $y$  is a ground truth image,  $\hat{y}$  is a corresponding generated image,  $\phi$  is a pre-trained model,  $j$  is the index of the layer in the pre-trained model used to generate the feature maps, and  $C_j$ ,  $H_j$ ,  $W_j$  are the number of channels, height, and width of each feature map.

For 3D images, two types of perceptual losses are widely applied: 3D perceptual loss and 2.5D perceptual loss. For 3D perceptual loss,  $D_j$ , the depth of each feature map is added to the equation above, and  $\phi$  becomes a 3D pre-trained model. Therefore, the 3D perceptual

loss becomes:

$$L_{3dperc}^{\phi,j}(\hat{y}, y) = \frac{1}{C_j H_j W_j D_j} \|\phi_j(\hat{y}) - \phi_j(y)\|_2^2 \quad (2)$$

There is also a 2.5D approach that aggregates 2D perceptual losses retrieved from three directions (axial, coronal, sagittal) using a pre-trained 2D model such as VGG (Ha et al., 2024). In other words, 2.5D perceptual loss slices the 3D images into axial, coronal, and sagittal slides, then gets the average or sum of 2D axial, coronal, and sagittal perceptual losses. Perceptual losses could also be used in Generative Adversarial Network (GAN)-based models (Javed et al., 2019; Qu et al., 2018).

### 2.3. Cross-Modality Brain Image Synthesis with Deep Learning

Cross-modality image synthesis involves learning the relationship between the input and the corresponding output to generate output-like images from the given input images. For brain images, the primary goal of cross-modality image synthesis tasks is generating realistic synthetic images in different modalities (e.g., MRI, PET, CT) or types (e.g., T1-weighted, T2-weighted) from available ones.

It is clinically meaningful as most medical imaging may reduce scanner time and imaging expenses, and deep learning enables high performance despite the necessity of complex nonlinear mapping between the modalities (Dayarathna et al., 2023). Multiple backbone models such as CycleGAN (Zhu et al., 2017) (e.g., Yang et al. (2018), Abu-Srhan et al. (2021)), U-Net (Ronneberger et al., 2015) (e.g., Sikka et al. (2018)) and Denoising Diffusion Probabilistic Models (Ho et al., 2020) (e.g., Pan et al. (2023), Xie et al. (2023)), are used. Some approaches encapsulate perceptual loss or similar loss as a part of their combined loss (Armanious et al., 2019; Dar et al., 2019).

There are many approaches to translating medical images to PET images as well. GAN-DALF (Shin et al., 2020) proposed Conditional Generative Adversarial Networks (CGAN) with discriminator-adaptive loss fine tuning to both synthesise T1w MRI images to  $^{18}\text{F}$ AV-45 and  $^{18}\text{F}$ FDG PET images and classify AD. BPGAN (Zhang et al., 2022) demonstrated T1w MRI to  $^{18}\text{F}$ FDG PET image translation using Conditional Variational Autoencoder GAN (cVAE-GAN) and conditional latent regressor GAN (cLR-GAN) with multiple loss functions including SSIM loss. TauPETGen is a latent diffusion model-based approach to generate  $^{18}\text{F}$ MK-6420 PET from text-written MMSE values and/or an MRI image (Jang et al., 2023).

### 2.4. U-Net

U-Net, a variant of autoencoder, was initially suggested for segmentation of medical images in 2015 (Ronneberger et al., 2015). It consists of a contracting path (encoder) and an expansive path (decoder). The feature maps pass through a 3x3 convolution and a ReLU activation twice for each encoder step and are downsampled using 2x2 max pooling. In the decoder, the maps are upsampled through 2x2 up-convolution, concatenated with the corresponding feature map from the encoder through a skip connection between encoder and decoder, and then pass through two 3x3 convolutions, each followed by a ReLU activation

for each step. The skip connections help maintain spatial information lost during encoding by providing pre-encoding information.

### 3. Methods

#### 3.1. Data Collection and Statistics

We collected 516 T1w MRI-Tau PET image pairs of 372 subjects from the Alzheimer’s Disease Neuroimaging Initiative (ADNI) dataset (adni.loni.usc.edu), specifically from ADNI-3. The retrieval time differences in all the pairs are less than a year, and all subjects are labelled as either AD, LMCI, MCI, or EMCI. The collected T1w MRI scans are all original images, and all the collected PET images are preprocessed and classified as ”AV1451 Coreg, Avg, Std Img and Vox Siz, Uniform 6mm Res”. For all the PET images, the tracer is [<sup>18</sup>F]AV-1451. Amongst them, we divide the dataset into train:validation:test = 360:78:78 in data preprocessing processes. The distribution of the pairs is demonstrated in Table 1.

Data Split	Male	Female	Age (Min-Max)	Race (White/Black/Others)	Diagnosis (AD/EMCI/MCI/LMCI)
Total (516)	291	225	74.2±7.9 (55.3-94.0)	462/31/23	97/102/267/50
Train (360)	206	154	73.9±8.0 (55.3-94.0)	321/22/17	66/70/187/37
Validation (78)	41	37	75.5±7.5 (59.4-91.6)	69/4/5	16/15/39/8
Test (78)	44	34	74.7±7.5 (57.4-92.0)	72/5/1	15/17/41/5

Table 1: Participants’ demographic and clinical characteristics. For the total, training, validation, and test datasets, information on gender, age, race, and clinical type (AD, EMCI, MCI, LMCI) is given. The ages are based on the MRI retrieval timestamp.

#### 3.2. Data Preprocessing

We converted the downloaded MRI and PET image files from ADNI from DICOM to NIFTI format by using a python library *dicom2nifti* (Brys, 2023) and divided them into train, test, and validation sets where they contain 360, 78, 78 MRI-PET pairs, respectively. We applied nonparametric non-uniformity intensity (N3) normalisation (Sled et al., 1998) with *mri\_nu\_correct.mni* and initial intensity normalisation (Dale et al., 1999) with *mri\_normalize* via Freeserfer (version 7.4.1) (The General Hospital Corporation (MGH), 2023), a software package specialised for analysing and visualising neuroimages such as MRI and PET.

After the normalisation processes, we performed a trimming step for MRI images to standardise the dimensions into cubic ( $x^3$ ) forms. We observed that the slices with very small or large indices contained nearly minimal voxel values, indicating a lack of relevant anatomical information. We removed slices based on the smallest dimension among the width, height, and depth of the scans to prevent them from being squashed when resizing them into 128x128x128 in the later stage. For instance, for an MRI image with a size of

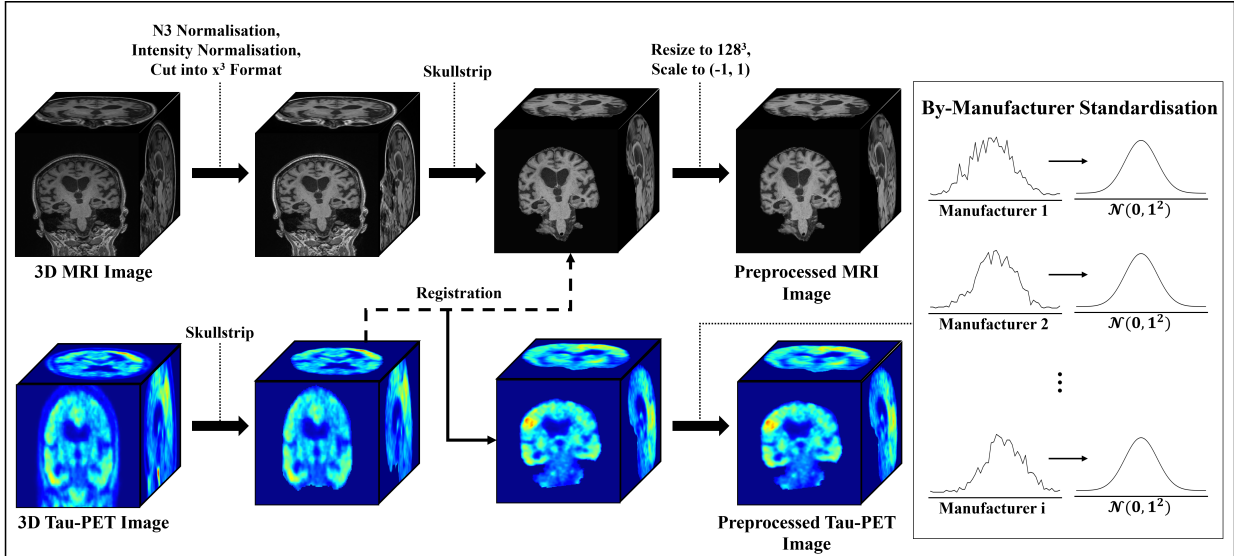


Figure 2: Overall data preprocessing procedures for MRI images and the corresponding tau-PET images. Nonparametric non-uniformity intensity (N3) normalisation and Freesurfer intensity normalisation are applied to the MRI images, and the MRI images are cut into cube format. Then, unnecessary tissues and skulls are removed from both MRI and PET images. After that, the PET images are registered to the MRI images. The voxel intensities of each MRI image are scaled into (0, 1). For PET images, voxel intensities from PET images with the same PET scanner manufacturer are standardised with a mean of 0 and a standard deviation of 1.

170x187x180, we adjusted it to a 170x170x170 format by removing slices from the coronal plane from index 0 to 8 and index 180 to 187 and from the coronal plane from index 0 to 4 and index 184 to 187.

The skulls are stripped from both MRI and PET images by applying Synthstrip (Hoopes et al., 2022) using the command *mri\_synthstrip* via Freesurfer. Then, PET images are registered to the corresponding MRI images by generating registration lta files using Freesurfer’s *mri\_coreg* command and resampling the PET volumes according to the generated lta files using Freesurfer’s *mri\_vol2vol* command. As a result, each PET image’s size naturally follows the MRI image’s size. After the registration, all the images are resized to a size of 128x128x128. Then, the MRI image’s intensity is normalised into (-1, 1) using min-max normalisation.

We reached the idea that min-max normalisation might blur or remove high-intensity areas (“hot spots”) for PET images. Also, we were unsure whether performing global-level normalisation (e.g., performing min-max normalisation based on a single maximum intensity and a single minimum intensity from multiple images). Although the 99-percentile intensity value of images from AD subjects is higher than MCI, EMCI, and LMCI subjects within the subjects scanned with scanners from the same manufacturer, there are significant statistical differences in intensity distributions between images from different PET manufacturers. Therefore, we standardised the preprocessed PET images with mean=0 and standard deviation=1 by each manufacturer retrieved from the metadata.

### 3.3. Data Augmentation

Data augmentations are performed randomly with their given probabilities for every epoch to provide the robustness of the model.

We applied 3D random elastic deformation with *monai.transforms.Rand3DElasticd* from MONAI (version 1.2.0), a Python library for Medical Artificial Intelligence (Cardoso et al., 2022). We use trilinear interpolation mode, magnitude range of (50, 100), 'zero' as a reflection mode, and Gaussian kernel's sigma range of (4, 7), with a probability of 0.5.

We also used random affine transformation with *monai.transforms.RandAffined* from MONAI. For each axis (x, y, z), an image is rotated between -15 to 15 degrees, scaled within a range of  $\pm 10\%$ , with a probability of 0.5. Random flip is applied for every axis through *monai.transforms.RandFlipd* from MONAI, with a probability of 0.5. 3D random elastic deformation, random affine transformation, and random flip are applied in the same manner for each MRI-PET pair.

Gaussian noise with mean=0 and standard deviation=1 is applied to every image to make the model robust against MRI artifacts or noise. It is applied to MRI images only.

### 3.4. Cyclic 2.5D Perceptual Loss

The combined Loss function consists of MSE, SSIM Loss, and cyclic 2.5D perceptual loss with hyperparameters  $\alpha$ ,  $\beta$ , and  $\gamma$ , thus represented as:

$$Loss_{combined}^{VGG16,23}(\hat{y}, y) = \alpha \times MSE(\hat{y}, y) + \beta \times L_{SSIM}(\hat{y}, y) + \gamma \times L_{perc}^{plane,VGG16,23}(\hat{y}, y) \quad (3)$$

Where  $\hat{y}$ ,  $y$  are the ground truth tau-PET image and the corresponding generated tau-PET image from the T1w MRI image.

The Cyclic 2.5D perceptual loss is implemented by sequentially applying the axial 2D average perceptual loss for a specified number of epochs, followed by the coronal 2D average perceptual loss for an equivalent number of epochs, and subsequently the sagittal 2D average perceptual loss for the same number of epochs. This sequence constitutes a single complete cycle, which keeps repeating with reduced intervals. We calculate 2D perceptual loss as described in Algorithm 1, but it differs from the original perceptual loss explained in section 2.2; it does not have  $\frac{1}{C_j H_j W_j D_j}$ . Since all the input data sizes are identical (128x128x128) and the same model's 23rd layer's output feature maps are used,  $C_j$ ,  $H_j$ ,  $W_j$ , and  $D_j$  are always the same regardless of the input data; thus,  $\frac{1}{C_j H_j W_j D_j}$  could be considered as a constant, so we do not need the term because the result is multiplied to *gamma* in the combined loss function.

$L_{perc}^{plane,VGG16,23}(\hat{y}, y)$  is a plane-based perceptual loss derived from the 23rd layer of the pre-trained VGG-16 model (i.e., the fourth convolution block's last layer excluding the Max Pooling layer). For each ground truth PET-generated PET pair,  $L_{perc}^{plane,VGG16,23}(\hat{y}, y)$  is calculated as follows pseudocode described in Algorithm 1 and Figure 3 below.

Initially, the plane is selected as axial, changed to sagittal, coronal, and repeated. The plane selection change interval ('interval' in Figure 2) keeps decreasing as the 'cycle' of axial,



---

**Algorithm 1** Pseudo-code for computing cyclic 2.5D perceptual loss

---

**Require:** The first 23 layers of a pre-trained VGG16 model  $VGG16_{23}$ ;

ground truth PET tensor  $y \in \mathbf{R}^{W \times D \times H}$ ;

generated PET tensor  $\hat{y} \in \mathbf{R}^{W \times D \times H}$ ;

mean squared error MSE; selected plane  $plane$  from algorithm 2

**Ensure:** Cyclic 2.5D perceptual loss  $L_{perc}^{plane, VGG16, 23}(y, \hat{y})$

Get  $y_i, \hat{y}_i \leftarrow SLICE(y, \hat{y}; plane)$  for  $i = 1..128$

$perceptual\_loss = 0$

**for**  $i = 1..128$  **do**

Min-Max Normalise  $y_i, \hat{y}_i$  into  $(0, 1)$

$perceptual\_loss \leftarrow perceptual\_loss + MSE(VGG16_{23}(y_i), VGG16_{23}(\hat{y}_i))$

**end for**

**return**  $perceptual\_loss/128$

---

coronal, and sagittal selection repeats. The interval stops decreasing in the later stages to prevent deactivating early stopping. The detailed description is in Algorithm 2 below. The interval becomes smaller in the later stages, but at a certain point, it should be the same so that early stopping is still usable in the later stages. We determined the selection change points based on Algorithm 2 below.

SSIM is a metric that evaluates statistical similarity based on luminance and contrast (Wang et al., 2004). When the window size is determined (11 in usual), a Gaussian filter with standard deviation  $\sigma$  is applied, and the window scans through both images  $\hat{y}, y$ . For the window pair of the images, means  $\mu_{\hat{y}}, \mu_y$ , variances  $\sigma_{\hat{y}}, \sigma_y$ , and the covariance  $\sigma_{\hat{y}y}$  are calculated, then SSIM is calculated as:

$$SSIM(\hat{y}, y) = \frac{(2\mu_{\hat{y}}\mu_y + C_1)(2\sigma_{\hat{y}y} + C_2)}{(\mu_{\hat{y}}^2 + \mu_y^2 + C_1)(\sigma_{\hat{y}}^2 + \sigma_y^2 + C_2)} \quad (4)$$

Where  $C_1 = (k_1 \cdot L)^2$ ,  $C_2 = (k_2 \cdot L)$ ,  $L$  is the data range, and  $k_1$  &  $k_2$  are usually set as 0.01 and 0.03 in default. Once the windows finish wandering over the image, it returns the average SSIM value. The window also has the same number of dimensions as images. For example, if the window size is 11 and the images are 3D, the window becomes (11x11x11).

SSIM can also be utilised as a loss function. In this context, the equation becomes:

$$L_{SSIM}(\hat{y}, y) = 1 - SSIM(\hat{y}, y) \quad (5)$$

Also, MSE is derived as:

$$MSE(\hat{y}, y) = \sum_{i=1}^D \sum_{j=1}^H \sum_{k=1}^W \frac{1}{D \times H \times W} (\hat{y}_{ijk} - y_{ijk})^2 \quad (6)$$

### 3.5. Model

We use 3D U-Net (Çiçek et al., 2016), similar to the 2D U-Net described in section 2.4, but utilises 3D convolutions instead of the 2D ones for synthesising tau-PET from T1w MRI.

---

**Algorithm 2** Pseudo-code for deciding epoch numbers where the plane for algorithm 1 is changed from axial to coronal, from coronal to sagittal, and from sagittal to axial

**Require:** Initial interval until the selected plane in algorithm 1 is changed *interval*; maximum number of epochs *max\_epoch*;  
early stopping patience *early\_stopping\_patience*

**Ensure:** Lists of number of epochs that change the selected plane in algorithm 1 to axial (*axial\_list*), coronal (*coronal\_list*), and sagittal (*sagittal\_list*)

*axial\_list, coronal\_list, sagittal\_list* = [], [], []

*current\_num* = 0

*exit\_condition* = *False*

**while** *current\_num* < *max\_epoch* **do**

    Add *current\_num* to *axial\_list*

**if** (*current\_num* + *interval*) < *max\_epoch* **then**

        Add *current\_num* + *interval* to *coronal\_list*

**if** (*current\_num* + 2 × *interval*) < *max\_epoch* **then**

            Add *current\_num* + 2 × *interval* to *sagittal\_list*

**else**

*exit\_condition* = *True*

**end if**

**else**

*exit\_condition* = *True*

**end if**

*current\_num* ← *current\_num* + 3 × *interval*

**if** *interval* // 1.5 > *early\_stopping\_patience* **then**

*interval* ← *interval* // 1.5

**end if**

**end while**

**return** *axial\_list, coronal\_list, sagittal\_list*

---

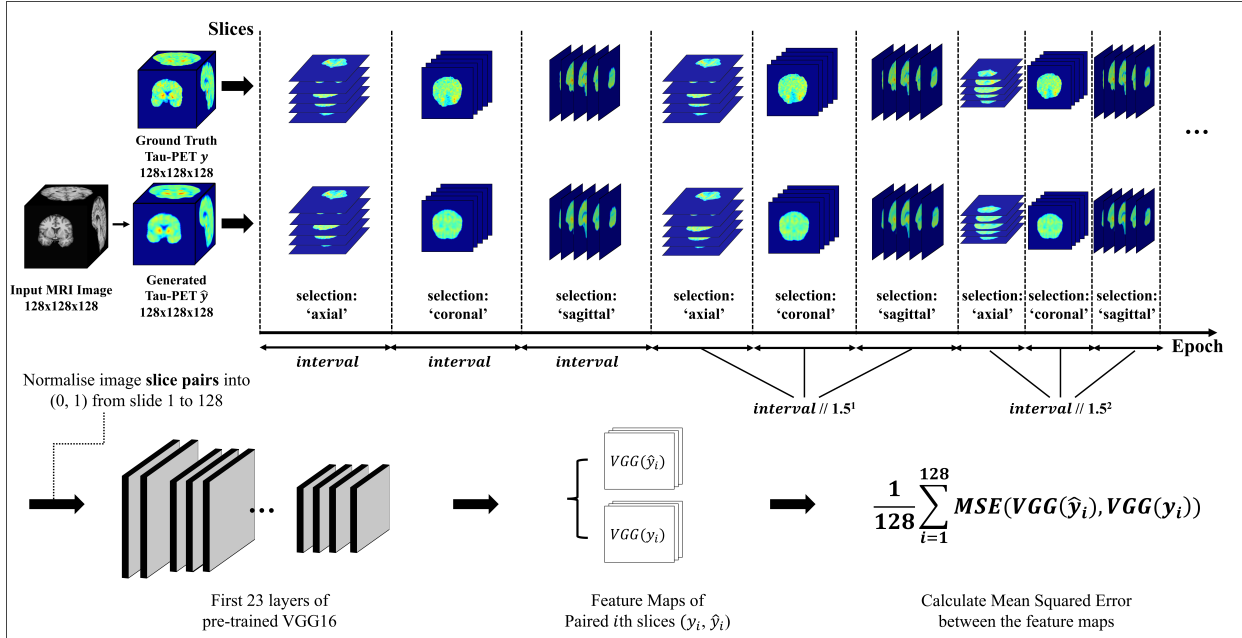


Figure 3: Overview of our proposed cyclic 2.5D perceptual loss. After generating a tau-PET image from the given MRI image, both ground truth tau-PET image and generated tau-PET image are sliced into axial, coronal, or sagittal images based on the number of epochs. The sliced image pairs (slice 1 to slice 128) are inputted in the first 23 layers of the pre-trained VGG16 model, and the corresponding feature maps are calculated. From the first slice pair to the 128th slice pair, the mean squared error within the paired feature maps is calculated and averaged.

We used instance normalisation (Ulyanov et al., 2016) instead of batch normalisation (Ioffe and Szegedy, 2015).

The goal is to generate a realistic 3D tau-PET image from a T1w MRI image, similar to the corresponding ground truth 3D tau-PET image. We use Adam optimiser (Kingma and Ba, 2014) with a cosine annealing scheduler (Loshchilov and Hutter, 2016). For each axial-coronal-sagittal routine, the period of the cosine annealing is set as equivalent to the interval in Algorithm 2 so that the learning rate is applied equally in each plane setting.

We also implement early stopping patience; thus, if the validation loss does not decrease for a certain number of epochs in each plane (axial, coronal, or sagittal), then the model stops execution. To avoid early stopping happening too early so that the model is overfitted to the specific plane, learning, early stopping is triggered only after the third 'round' of the axial-coronal-sagittal cycle.

We use the channel settings as (64, 128, 256, 512, 1024), maximum epoch number as 1000, and maximum learning rate as  $5e-4$  empirically. Dropout (Srivastava et al., 2014) of probability 0.2 is also applied to mitigate potential overfitting problems.

### 3.6. Experimental Settings

We created multiple datasets to check the effectiveness of our preprocessing procedures. One follows our preprocessing procedures, and the other uses min-max normalisation to (-1, 1) in the final PET normalisation step instead of standardisation. We also created a dataset processed without initial Freesurfer intensity normalisation on MRI (noFSNorm), a dataset processed without N3 normalisation and initial Freesurfer intensity normalisation (noN3FSNorm), and a dataset processed without skullstrip (noSkullStrip) so that we can visualise the effectiveness of each preprocessing steps. We created extra datasets to perform an ablation study for non-complex losses (MSE only, SSIM only) and a complex loss without the perceptual loss (MSE + SSIM).

For 3D U-Net with combined loss experiments, we also conducted combined loss with 2.5D and 3D perceptual losses. For 2.5D perceptual loss, we calculated axial, sagittal, and coronal-wise 2D perceptual losses and averaged them. For 3D perceptual loss, we used the pre-trained resnet10 medicalnet (Chen et al., 2019) model using *monai.losses.PerceptualLoss* from MONAI (version 1.3.0). Both 2.5D and 3D perceptual loss-based combined loss settings are tested on both datasets.

For any 2D-based perceptual approaches (2.5D, cyclic 2.5D perceptual loss), hyperparameters  $\alpha$ ,  $\beta$ , and  $\gamma$  are set as 0.25, 0.4, and 0.65, while they are determined as 0.25, 0.5, and 14.0 for 3D perceptual approaches, based on the empirical approaches.

The experiments were conducted primarily using NVIDIA RTX 6000 Ada (48GB VRAM). Multi-GPU training was used when experimenting with SwinUNETR. We utilised various available resources during the model development phase, including RTX A6000, RTX 6000 Ada, and A100.

As experiments with 2.5D or 3D perceptual loss do not require delayed early stopping, the early stopping was applied from the initial epoch for U-Net and U-Net variant experiments with those settings. For CycleGAN and Pix2Pix experiments, we did not apply the early stopping because early stopping based on the loss values for GAN-based models may cause unstable or low visual quality despite the low loss values. Additionally, CycleGAN and Pix2Pix experiments empirically used the maximum learning rate of  $2e-4$ .

## 4. Results

### 4.1. Results

We performed the synthesis of 3D tau-PET images from 3D T1w MRI images in two datasets: the dataset preprocessed with our method and the one that followed most of our method but used min-max normalisation into (-1, 1) for PET images instead of the suggested by-manufacturer normalisation). The tasks were performed with 3D U-Net, as demonstrated in section 3.5, with combined losses of MSE, SSIM loss, and perceptual loss. We used three different settings for perceptual loss: 2.5D perceptual loss, 3D perceptual loss (as introduced in section 4.1), and our proposed cyclic 2.5D perceptual loss. We evaluated the results with 3D average test SSIM, 3D average test PSNR, and 2D average Axial-, Coronal-, and

Dataset	Perceptual Loss	SSIM (mean±std)				PSNR (mean±std)			
		Overall (3D)	Axial	Coronal	Sagittal	Overall (3D)	Axial	Coronal	Sagittal
<b>Ours</b>	2.5D	0.897±0.037	0.855±0.045	0.856±0.044	0.844±0.047	28.183±2.830	29.214±4.250	26.944±2.678	27.380±3.010
	3D	0.894±0.039	0.853±0.047	0.853±0.046	0.840±0.049	28.428±2.592	29.017±3.528	27.164±2.443	27.477±2.718
	<b>Cyclic 2.5D (Ours)</b>	<b>0.900±0.036</b>	<b>0.859±0.044</b>	<b>0.861±0.042</b>	<b>0.848±0.046</b>	<b>28.728±2.631</b>	<b>29.638±3.931</b>	<b>27.469±0.044</b>	<b>27.827±2.828</b>
PET minmax norm	2.5D	0.881±0.052	<b>0.829±0.064</b>	0.829±0.066	0.815±0.072	27.041±2.573	27.135±2.572	25.674±2.534	25.875±2.662
	3D	0.853±0.052	0.810±0.064	0.809±0.066	0.799±0.071	25.628±1.829	25.172±1.785	24.655±1.983	24.708±2.051
	<b>Cyclic 2.5D (Ours)</b>	<b>0.882±0.051</b>	0.828±0.066	<b>0.830±0.065</b>	<b>0.817±0.071</b>	<b>27.321±2.448</b>	<b>27.506±2.825</b>	<b>25.928±2.443</b>	<b>26.187±2.559</b>

Table 2: Quantitative comparisons of image-to-image generation of 3D U-Net with a combined loss of MSE loss, SSIM loss, and different perceptual losses in dataset preprocessed with different methods. Note: Ours: dataset preprocessed with the proposed preprocessing method, PET minmax norm: dataset used min-max PET normalisation instead of by-manufacturer standardisation, Overall (3D): overall 3D PSNR or SSIM, Axial/Coronal/Sagittal: average 2D PSNR or SSIM for axial/coronal/sagittal slide 20 to 90. The experiments are conducted on the test dataset only.

Model	Perceptual Loss	SSIM (mean±std)				PSNR (mean±std)			
		Overall (3D)	Axial	Coronal	Sagittal	Overall (3D)	Axial	Coronal	Sagittal
U-Net	2.5D	0.897±0.037	0.855±0.045	0.856±0.044	0.844±0.047	28.183±2.830	29.214±4.250	26.944±2.678	27.380±3.010
	3D	0.894±0.039	0.853±0.047	0.853±0.046	0.840±0.049	28.428±2.592	29.017±3.528	27.164±2.443	27.477±2.718
	<b>Cyclic 2.5D (Ours)</b>	<b>0.900±0.036</b>	<b>0.859±0.044</b>	<b>0.861±0.042</b>	<b>0.848±0.046</b>	<b>28.728±2.631</b>	<b>29.638±3.931</b>	<b>27.469±2.439</b>	<b>27.827±2.828</b>
UNETR	2.5D	0.891±0.037	0.848±0.044	0.848±0.043	0.836±0.046	<b>28.234±2.187</b>	28.951±3.391	<b>26.982±1.940</b>	27.363±2.342
	3D	0.895±0.037	0.854±0.045	0.854±0.044	0.842±0.047	27.943±2.610	28.636±3.615	26.728±2.517	27.055±2.751
	<b>Cyclic 2.5D (Ours)</b>	<b>0.896±0.034</b>	<b>0.854±0.042</b>	<b>0.855±0.041</b>	<b>0.843±0.044</b>	28.171±2.517	<b>29.236±3.855</b>	26.893±2.325	<b>27.458±2.731</b>
SwinUNETR	2.5D	0.898±0.036	0.857±0.043	0.858±0.042	0.845±0.046	28.313±2.178	28.987±3.252	27.064±1.959	24.438±2.345
	3D	0.897±0.038	0.857±0.046	0.857±0.045	0.845±0.048	<b>28.429±2.626</b>	29.094±3.608	<b>27.247±2.327</b>	<b>27.543±2.738</b>
	<b>Cyclic 2.5D (Ours)</b>	<b>0.899±0.038</b>	<b>0.860±0.046</b>	<b>0.862±0.044</b>	<b>0.847±0.048</b>	28.345±2.833	<b>29.227±3.835</b>	27.188±2.587	27.447±2.991
CycleGAN	Original	0.843±0.052	0.788±0.060	0.782±0.059	0.766±0.062	25.500±2.297	25.784±3.246	24.173±2.202	24.448±2.504
	2.5D	<b>0.862±0.043</b>	0.806±0.051	0.806±0.049	0.788±0.054	<b>26.661±2.195</b>	<b>27.134±3.174</b>	<b>25.318±2.041</b>	<b>25.701±2.431</b>
	3D	0.855±0.046	0.801±0.053	0.797±0.052	0.780±0.056	26.317±2.146	26.950±3.160	24.995±1.989	25.391±2.362
Pix2Pix	Original	0.861±0.041	0.808±0.047	0.810±0.046	0.792±0.050	26.670±2.167	27.050±2.991	25.341±1.937	25.555±2.255
	2.5D	0.875±0.039	0.824±0.046	0.824±0.044	0.807±0.049	27.264±2.462	27.977±3.535	25.993±2.236	26.279±2.537
	3D	0.865±0.044	0.816±0.051	0.814±0.050	0.798±0.053	26.173±2.073	26.837±3.016	24.840±1.955	25.171±2.337
<b>Cyclic 2.5D (Ours)</b>	<b>0.886±0.044</b>	<b>0.846±0.049</b>	<b>0.845±0.049</b>	<b>0.831±0.053</b>	<b>27.686±2.408</b>	<b>28.159±3.114</b>	<b>26.485±2.220</b>	<b>26.749±2.543</b>	

Table 3: Quantitative comparisons of image-to-image generation of 3D U-Net, 3D UNETR, 3D SwinUNETR, CycleGAN, Pix2Pix with original loss (CycleGAN, Pix2Pix only) and our proposed combined loss with 2.5D, 3D, and cyclic 2.5D perceptual loss in dataset preprocessed with our proposed method. Note: Overall (3D): overall 3D PSNR or SSIM, Axial/Coronal/Sagittal: average 2D PSNR or SSIM for axial/coronal/sagittal slide 20 to 90. The experiments are conducted on the test dataset only.

Sagittal-wise test SSIM & PSNR. For 2D metrics, slides 20 to 90 were used so that the most meaningful slides were exclusively included in the calculation.

For 3D average PSNR and SSIM, our cyclic 2.5D perceptual loss outperformed others regardless of the dataset. In our dataset, cyclic 2.5D perceptual loss outperformed other perceptual losses in all axial, sagittal, and coronal-wise average 2D PSNR and SSIM. In the dataset setting with min-max PET normalisation, it outmatched others in all metrics, excluding axial-side SSIM. Sample axial-side test images are displayed in Figure 4.

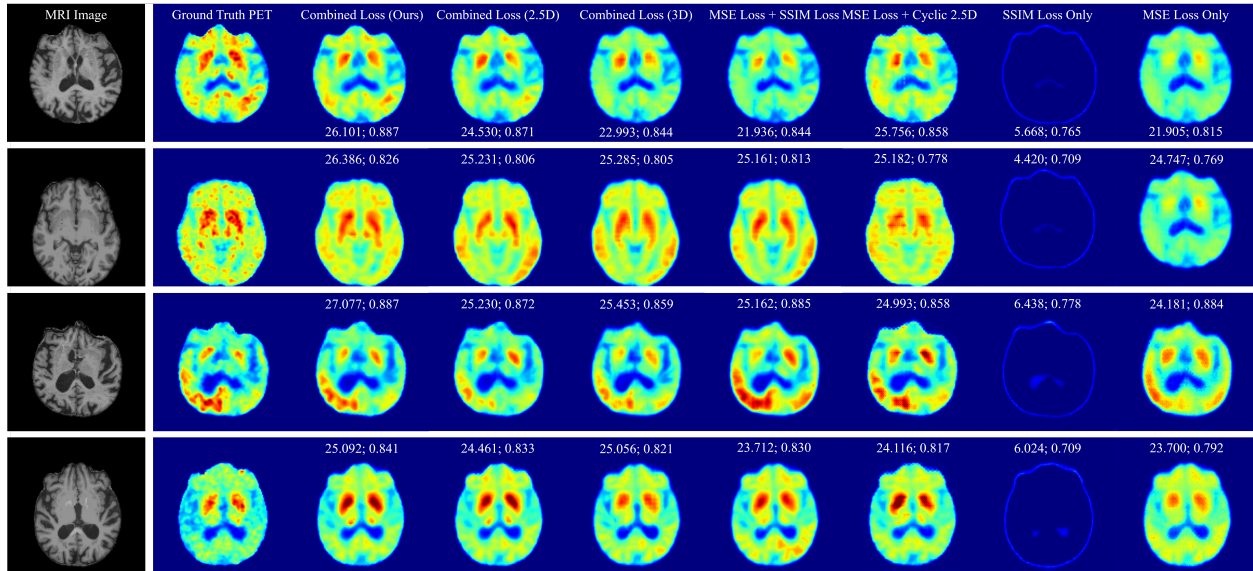


Figure 4: Qualitative comparison of images generated by 3D U-Net with different loss values. The first column demonstrates the input MRI images, the second illustrates the ground truth PET images, and the others display the generated images. The PSNR and SSIM values between the ground truth PET and the generated images are shown from column 3 to the final column.

There are several samples with inconsistent alignments between the SSIM and PSNR values and the visual quality of the generated PET images. We demonstrate some axial-side examples in Figure 5. The metrics in Figure 5 are the slide’s 2D PSNR or SSIM.

Our proposed combined loss of MSE, SSIM loss, and cyclic 2.5D perceptual loss is readily applicable to any generative model if it has paired ground truth image and generative image. We applied the combined loss with 2.5D perceptual loss, with 3D perceptual loss, and with our proposed perceptual cyclic 2.5D perceptual loss to other U-Net-like models, UNETR (Hatamizadeh et al., 2022) and SwinUNETR (Hatamizadeh et al., 2021), and well-known generative models, Pix2Pix (Isola et al., 2017) and CycleGAN Zhu et al. (2017).

Both Pix2Pix and CycleGAN are based on GAN, a generative model where a generator, which creates data from noise, and a discriminator, which classifies the true data and the fake data, compete with each other (Goodfellow et al., 2014). CycleGAN is a type of GAN-based neural network that enables image-to-image translation whose loss consists of adversarial loss (ensure that a generated image is indistinguishable from the real one), cycle consistency loss (ensure that an image remains unchanged when the image is synthesised to another domain and return to the original domain), and an identity loss (ensure that an image remains unchanged when an image from the target domain is inputted into the generator). Pix2Pix is also a GAN-variant image-to-image translation model whose loss includes adversarial loss (for a similar purpose as CycleGAN’s adversarial loss) and L1 loss (ensure that the pixel-level difference between a true image and the corresponding generated image is minimised). For CycleGAN and Pix2Pix, we tested the models with the original losses and modified losses with our proposed combined loss with cyclic 2.5D perceptual loss. We added our loss to CycleGAN’s original loss while replacing the L1 loss with our loss for Pix2Pix. We also

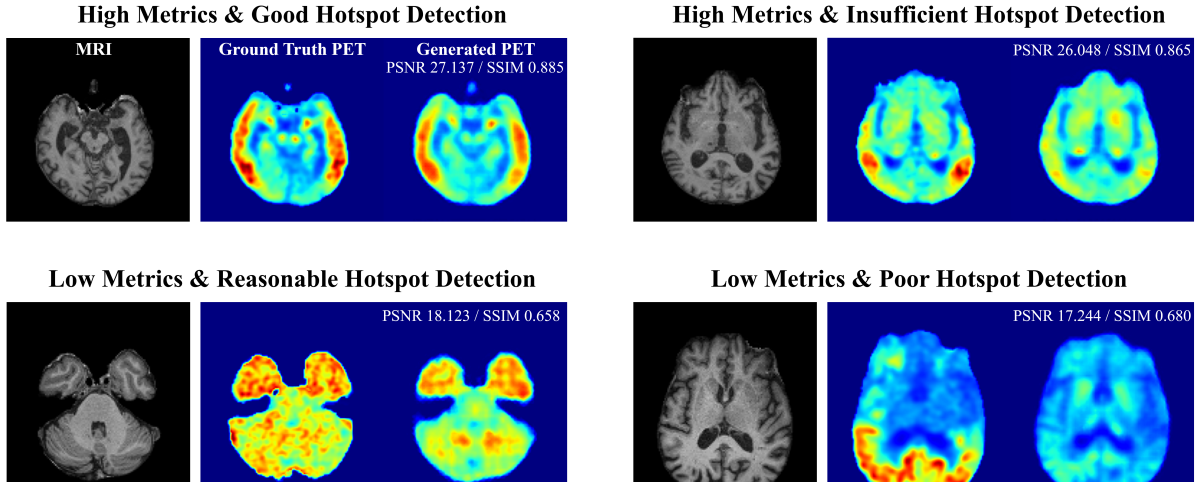


Figure 5: Multiple pairs of an input MRI image, the corresponding ground truth tau-PET image, and the generated tau-PET image. The top-left and bottom-right pairs demonstrate a consistent alignment between the metrics and detection of visual hot spots (regions of high voxel intensities of the ground truth tau-PET images). However, the top-right and bottom-left pairs display that the metrics did not adequately reflect the visual hot spot detection.

tested with similar modified losses with 2.5D and 3D perceptual losses. The results are demonstrated in Table 3.

#### 4.2. Ablation Study

Loss Function	SSIM				PSNR			
	Overall (3D)	Axial	Coronal	Sagittal	Overall (3D)	Axial	Coronal	Sagittal
SSIM	0.811±0.051	0.715±0.072	0.725±0.063	0.688±0.070	4.750±2.027	12.080±3.114	10.149±2.006	11.075±2.352
MSE	0.885±0.036	0.841±0.044	0.842±0.042	0.828±0.045	28.321±2.354	28.522±2.948	27.039±2.218	27.236±2.422
SSIM+MSE	0.897±0.037	0.856±0.045	0.856±0.044	0.844±0.047	28.110±2.614	28.809±3.644	26.853±2.474	27.191±2.745
MSE+Perceptual	0.887±0.037	0.844±0.045	0.846±0.043	0.828±0.047	28.228±2.502	28.508±3.133	26.975±2.355	27.193±2.584
Perceptual+SSIM+MSE (Ours)	<b>0.900±0.036</b>	<b>0.859±0.044</b>	<b>0.861±0.042</b>	<b>0.848±0.046</b>	<b>28.728±2.631</b>	<b>29.638±3.931</b>	<b>27.469±2.439</b>	<b>27.827±2.828</b>

Table 4: Quantitative comparisons of image-to-image generation of 3D U-Net with SSIM loss only, MSE loss only, a combination of SSIM loss and MSE Loss (i.e., no perceptual loss), a combination of MSE loss and cyclic 2.5D perceptual loss (i.e., our loss without SSIM loss), and our proposed combined loss in dataset preprocessed with our proposed method. Note: Overall (3D): overall 3D PSNR or SSIM, Axial/Coronal/Sagittal: average 2D PSNR or SSIM for axial/coronal/sagittal slide 20 to 90. The experiments are conducted on the test dataset only.

We also tested the 3D generative U-Net model with SSIM loss only, MSE loss only, combined MSE and SSIM loss, and combined MSE and cyclic 2.5D perceptual loss for dataset preprocessed with our method. Also, we applied a 3D generative U-Net model with the proposed combined loss to noFSNorm (similar to our dataset, but without initial MRI intensity normalisation), noN3FSNorm (without MRI N3 normalisation and initial MRI intensity normalisation), and noSkullStrip (without skull and unnecessary tissue removal process) The results are displayed in Table 5.

Dataset	SSIM				PSNR			
	Overall (3D)	Axial	Coronal	Sagittal	Overall (3D)	Axial	Coronal	Sagittal
noFSNorm	0.899±0.036	0.858±0.045	0.859±0.043	0.847±0.046	28.427±2.781	29.307±4.058	27.171±2.612	27.551±2.909
noN3FSNorm	0.898±0.036	0.857±0.044	0.859±0.043	0.846±0.046	28.395±2.744	29.363±4.150	27.153±2.544	27.525±2.897
noSkullStrip	0.814±0.054	0.768±0.056	0.776±0.054	0.755±0.054	27.558±2.216	27.345±2.892	26.673±2.115	26.168±2.178
Ours	<b>0.900±0.036</b>	<b>0.859±0.044</b>	<b>0.861±0.042</b>	<b>0.848±0.046</b>	<b>28.728±2.631</b>	<b>29.638±3.931</b>	<b>27.469±2.439</b>	<b>27.827±2.828</b>

Table 5: Quantitative comparisons of image-to-image generation of 3D U-Net and our proposed combined loss in dataset preprocessed with our proposed method and the ones with different missing steps. Note: noFSNorm: No initial Freesurfer intensity normalisation on MRI, noN3FSNorm: No N3 normalisation & Freesurfer intensity normalisation on MRI, noSkullstrip: No skull strip on both MRI and PET, Overall (3D): overall 3D PSNR or SSIM, Axial/Coronal/Sagittal: average 2D PSNR or SSIM for axial/coronal/sagittal slide 20 to 90. The experiments are conducted on the test dataset only.

When applied in conjunction with the 3D U-Net architecture, our proposed loss function performed better than both the individual and combined applications of the MSE and SSIM loss functions, as well as the combination of MSE and cyclic 2.5D perceptual loss. Additionally, the 3D U-Net model with the combined loss function demonstrated the best performance on the dataset processed using our proposed preprocessing methods, compared to the variations without initial MRI intensity normalisation, without MRI N3 normalisation and initial MRI intensity normalisation, and without skull and unnecessary tissue removal.

## 5. Discussion

Our study demonstrates that the proposed cyclic 2.5D perceptual loss mostly outperforms 2.5D and 3D perceptual losses when combined with MSE and SSIM losses in U-Net and U-Net variant experiments. Interestingly, although cyclic 2.5D perceptual loss uses single-plane (in our setting, axial plane unless early stopping is triggered) 2D perceptual loss for certain intervals at the end of the training, it generally outperforms in 3D and all the three planar 2D metrics. This finding can be likened to shaping a square with clay by patting each side. Initially, the clay does not resemble a cube, but as the process is repeated multiple times, it gradually approaches the desired shape. During training, the validation loss of the model using the proposed combined loss spiked when the plane was changed in the initial stages, but the magnitude of these spikes decreased as training progressed. Another potential reason for this finding is the avoidance of overfitting. The 2.5D perceptual loss, unlike our proposed method, aggregates all axial, coronal, and sagittal 2D perceptual losses. It may cause the generative model to focus on only one or two of the plane-wise perceptual losses, which are deemed ‘easier’ for the model. However, since the proposed loss treats all planes over the same number of epochs, this issue is less likely to occur.

As demonstrated in the experiments, the cyclic 2.5D perceptual loss is also easy to apply to GAN-based models such as CycleGAN and Pix2Pix. Notably, our loss resulted in improved 2D and 3D PSNR and SSIM values in the Pix2Pix image synthesis of tau-PET from T1w MRI; it not only outperformed the baseline loss function but also showed improved results across all metrics. This indicates the utility of both the cyclic 2.5D perceptual loss and the combined loss not only in U-Net-based models but also in other types of image synthesis models.



As we mentioned above, one of the reasons behind this improvement may be avoiding overfitting. Through continuous alternations of the 2D perceptual loss retrieval plane, the standard of evaluation regularly changes. Therefore, this may prevent the model from overfitting to one plane, allowing it to find a better optimum. This concept can be likened to the idea behind the cyclic learning rate (Smith, 2017). The cyclic learning rate cyclically changes the learning rate for deep learning-based classification models. When the learning rate is high, the magnitude of the update (or the step size) becomes large, allowing the model to escape saddle points more easily. Conversely, when the learning rate is low, the updates become more precise, enabling the model to approach the optimum accurately. Therefore, using a cyclic learning rate allows the model to explore broader parameter space and escape saddle points when the learning rate is high while meticulously fine-tuning the parameters as it approaches the optimum when the learning rate is low. This results in faster and more stable convergence than a fixed learning rate. For our cyclic 2.5D perceptual loss, the high learning rate moments could be understood as the first few epochs after changing the perceptual loss retrieval plane. If the model is not adapted to both previous and subsequent planes, it then tries to adjust itself for the subsequent plane’s perceptual quality. The model is meticulously tuned for the plane in the later epochs after the plane alternation. As the interval of the whole cycle becomes smaller, the model is gradually tuned for all the planes.

For CycleGAN, our proposed cyclic 2.5D perceptual loss approach did not outperform the conventional 2.5D one. This outcome might be attributed to two primary factors. First, a fundamental objective of CycleGAN is to maintain consistency during bidirectional modality conversion. The cyclic 2.5D perceptual loss periodically alters the 2D perceptual loss retrieval plane, which may introduce instability into the training process. Second, compared to other models we tested, CycleGAN’s framework comprises more submodels, specifically two generators and two discriminators. The rationale behind initially setting a large inner-cycle interval and gradually decreasing it is stabilising the training in the early cycles and allowing the model to consider various planes once the training is stabilised. However, due to the presence of more submodels within the CycleGAN framework, the initial interval might not have been sufficient to stabilise all components.

Despite the generally lower performance than the 2.5D perceptual loss approach for CycleGAN, incorporating the combined cyclic 2.5D perceptual loss resulted in better performance than the baseline loss across all metrics. Furthermore, it often secured a competitive follow-up performance even in metrics where it underperformed relative to the 2.5D perceptual loss. Additionally, the 2.5D perceptual loss configuration required approximately 1.8 times longer per epoch than our approach. Therefore, our proposed method proved to be effective and meaningful, even for the CycleGAN model.

Amongst our preprocessing, the standardisation of PET images by their manufacturers helped the model considerably compared to widely used min-max normalisation. The potential reason is that similar characteristics (e.g., AD has the highest 99-percentile voxel intensity value) occur in images retrieved from the scanners with the same manufacturer, but different voxel intensity distribution lies between images from different manufacturers.

Several images generated with high PSNR or SSIM values were of poor visual quality. This frequently occurred in PET images with predominantly low voxel intensity values but with a few prominent "hot spots", although not every image with this issue adhered to this pattern. It implies the limitations of traditional metrics used to evaluate the quality of generated PET images. Hence, a new metric that addresses this problem might be necessary.

Despite the benefits of our proposed cyclic 2.5D perceptual loss, it has a limitation. Since it considers all the slides when sliced, it may also include slides with nearly meaningless information. For instance, many slides at both ends contain almost no tissue, so MSE and SSIM losses are sufficient to address them. Future work needs to address this to maximise the benefits of perceptual loss and decrease computational time. Additionally, while traditional metrics like PSNR and SSIM are useful, they sometimes fail to reflect the true visual quality of generated images. This highlights the need to develop a new evaluation metric for PET image synthesis.

## 6. Conclusion

In this study, we introduce a novel cyclic 2.5D perceptual loss function for 3D environments and incorporate it with MSE loss and SSIM loss for effective 3D image synthesis of tau-PET images from T1w MRI images. The proposed loss effectively captures perceptual information from all planes without overfitting to limited planes. Recognising the imbalanced distribution of voxel intensities in tau-PET images from different scanner manufacturers, we suggest by-manufacturer PET standardisation. To evaluate our approach, we conduct multiple experiments on various neural network models using paired T1w MRI and tau-PET 3D images from the ADNI database. Both qualitative and quantitative results prove the effectiveness of the proposed loss and its expandability to other synthesis models. The ablation study illustrates that the suggested PET standardisation aids the neural network models better than min-max PET normalisation. We also demonstrate the necessity of developing advanced cyclic 2.5D perceptual loss computed based on slides containing meaningful information only and a new evaluation metric tailored to PET image synthesis. The proposed method has the potential to contribute to the early diagnosis of AD by synthesising high-quality tau-PET images from more accessible T1w MRI images.

## CRedit authorship contribution statement

**Kim, S.:** Methodology, Data curation, Formal Analysis, Investigation, Software, Visualization, Writing – original draft, Writing – Review & Editing. **Moon, J.:** Software, Validation, Writing – Review & Editing. **Chung, H.:** Funding acquisition, Resources, Writing – Review & Editing. **Jang, I.:** Conceptualization, Methodology, Formal Analysis, Funding acquisition, Resources, Supervision, Writing – Review & Editing.

## Acknowledgements

The authors appreciate Chanik Kang, Daehwan Kim, and Jiwoong Yang for providing valuable feedback on drafting and editing the paper. This work was supported by the National Supercomputing Center with supercomputing resources including technical support

(KSC-2024-CRE-0021), Hankuk University of Foreign Studies Research Fund of 2024, the National Research Foundation of Korea (NRF) grant funded by the Ministry of Science and ICT (MSIT) (RS-2024-00338048), the Global Research Support Program in the Digital Field program and Artificial Intelligence Graduate School Program of Hanyang University (RS-2024-00412644, RS-2020-II201373) supervised by the Institute of Information and Communications Technology Planning & Evaluation (IITP), and the Culture, Sports and Tourism R&D Program through the Korea Creative Content Agency grant funded by the Ministry of Culture, Sports and Tourism in 2024(RS-2024-00332210). Data collection and sharing for the Alzheimer’s Disease Neuroimaging Initiative (ADNI) is funded by the National Institute on Aging (National Institutes of Health Grant U19 AG024904). The grantee organisation is the Northern California Institute for Research and Education. In the past, ADNI has also received funding from the National Institute of Biomedical Imaging and Bioengineering, the Canadian Institutes of Health Research, and private sector contributions through the Foundation for the National Institutes of Health (FNIH) including generous contributions from the following: AbbVie, Alzheimer’s Association; Alzheimer’s Drug Discovery Foundation; Araclon Biotech; BioClinica, Inc.; Biogen; Bristol-Myers Squibb Company; CereSpir, Inc.; Cogstate; Eisai Inc.; Elan Pharmaceuticals, Inc.; Eli Lilly and Company; EuroImmun; F. Hoffmann-La Roche Ltd and its affiliated company Genentech, Inc.; Fujirebio; GE Healthcare; IXICO Ltd.; Janssen Alzheimer Immunotherapy Research & Development, LLC.; Johnson & Johnson Pharmaceutical Research & Development LLC.; Lumosity; Lundbeck; Merck & Co., Inc.; Meso Scale Diagnostics, LLC.; NeuroRx Research; Neurotrack Technologies; Novartis Pharmaceuticals Corporation; Pfizer Inc.; Piramal Imaging; Servier; Takeda Pharmaceutical Company; and Transition Therapeutics.

## References

- Abu-Srhan, A., Almallahi, I., Abushariah, M.A., Mahafza, W., Al-Kadi, O.S., 2021. Paired-unpaired unsupervised attention guided gan with transfer learning for bidirectional brain mr-ct synthesis. *Computers in Biology and Medicine* 136, 104763.
- Armanious, K., Jiang, C., Abdulatif, S., Küstner, T., Gatidis, S., Yang, B., 2019. Unsupervised medical image translation using cycle-medgan, in: 2019 27th European signal processing conference (EUSIPCO), IEEE. pp. 1–5.
- Brys, A., 2023. dicom2nifti. URL: <https://github.com/icometrix/dicom2nifti>. version 2.4.8.
- Bucci, M., Chiotis, K., Nordberg, A., Initiative, A.D.N., 2021. Alzheimer’s disease profiled by fluid and imaging markers: tau pet best predicts cognitive decline. *Molecular Psychiatry* 26, 5888–5898.
- Buchhave, P., Minthon, L., Zetterberg, H., Wallin, Å.K., Blennow, K., Hansson, O., 2012. Cerebrospinal fluid levels of  $\beta$ -amyloid 1-42, but not of tau, are fully changed already 5 to 10 years before the onset of alzheimer dementia. *Archives of general psychiatry* 69, 98–106.

- Cardoso, M.J., Li, W., Brown, R., Ma, N., Kerfoot, E., Wang, Y., Murray, B., Myronenko, A., Zhao, C., Yang, D., Nath, V., He, Y., Xu, Z., Hatamizadeh, A., Zhu, W., Liu, Y., Zheng, M., Tang, Y., Yang, I., Zephyr, M., Hashemian, B., Alle, S., Zalbagi Darestani, M., Budd, C., Modat, M., Vercauteren, T., Wang, G., Li, Y., Hu, Y., Fu, Y., Gorman, B., Johnson, H., Genereaux, B., Erdal, B.S., Gupta, V., Diaz-Pinto, A., Dourson, A., Maier-Hein, L., Jaeger, P.F., Baumgartner, M., Kalpathy-Cramer, J., Flores, M., Kirby, J., Cooper, L.A., Roth, H.R., Xu, D., Bericat, D., Floca, R., Zhou, S.K., Shuaib, H., Farahani, K., Maier-Hein, K.H., Aylward, S., Dogra, P., Ourselin, S., Feng, A., 2022. MONAI: An open-source framework for deep learning in healthcare doi:<https://doi.org/10.48550/arXiv.2211.02701>.
- Chen, S., Ma, K., Zheng, Y., 2019. Med3d: Transfer learning for 3d medical image analysis. arXiv preprint arXiv:1904.00625 .
- Çiçek, Ö., Abdulkadir, A., Lienkamp, S.S., Brox, T., Ronneberger, O., 2016. 3d u-net: learning dense volumetric segmentation from sparse annotation, in: Medical Image Computing and Computer-Assisted Intervention–MICCAI 2016: 19th International Conference, Athens, Greece, October 17-21, 2016, Proceedings, Part II 19, Springer. pp. 424–432.
- Dale, A.M., Fischl, B., Sereno, M.I., 1999. Cortical surface-based analysis: I. segmentation and surface reconstruction. *Neuroimage* 9, 179–194.
- Dar, S.U., Yurt, M., Karacan, L., Erdem, A., Erdem, E., Cukur, T., 2019. Image synthesis in multi-contrast mri with conditional generative adversarial networks. *IEEE transactions on medical imaging* 38, 2375–2388.
- Dayarathna, S., Islam, K.T., Uribe, S., Yang, G., Hayat, M., Chen, Z., 2023. Deep learning based synthesis of mri, ct and pet: Review and analysis. *Medical Image Analysis* , 103046.
- Delbeke, D., Coleman, R.E., Guiberteau, M.J., Brown, M.L., Royal, H.D., Siegel, B.A., Townsend, D.W., Berland, L.L., Parker, J.A., Hubner, K., et al., 2006. Procedure guideline for tumor imaging with 18f-fdg pet/ct 1.0. *Journal of nuclear Medicine* 47, 885–895.
- Dosovitskiy, A., Brox, T., 2016. Generating images with perceptual similarity metrics based on deep networks. *Advances in neural information processing systems* 29.
- van der Flier, W.M., de Vugt, M.E., Smets, E.M., Blom, M., Teunissen, C.E., 2023. Towards a future where alzheimer’s disease pathology is stopped before the onset of dementia. *Nature aging* 3, 494–505.
- Goodfellow, I., Pouget-Abadie, J., Mirza, M., Xu, B., Warde-Farley, D., Ozair, S., Courville, A., Bengio, Y., 2014. Generative adversarial nets. *Advances in neural information processing systems* 27.
- Guo, Y., Huang, Y.Y., Shen, X.N., Chen, S.D., Hu, H., Wang, Z.T., Tan, L., Yu, J.T., Initiative, A.D.N., 2021. Characterization of alzheimer’s tau biomarker discordance using plasma, csf, and pet. *Alzheimer’s research & therapy* 13, 93.

- Ha, J., Wang, N., Maharjan, S., Zhang, X., 2024. 3d volumetric super-resolution in radiology using 3d rrdg-gan. arXiv preprint arXiv:2402.04171 .
- Hatamizadeh, A., Nath, V., Tang, Y., Yang, D., Roth, H.R., Xu, D., 2021. Swin unetr: Swin transformers for semantic segmentation of brain tumors in mri images, in: International MICCAI Brainlesion Workshop, Springer. pp. 272–284.
- Hatamizadeh, A., Tang, Y., Nath, V., Yang, D., Myronenko, A., Landman, B., Roth, H.R., Xu, D., 2022. Unetr: Transformers for 3d medical image segmentation, in: Proceedings of the IEEE/CVF winter conference on applications of computer vision, pp. 574–584.
- He, K., Zhang, X., Ren, S., Sun, J., 2016. Deep residual learning for image recognition, in: Proceedings of the IEEE conference on computer vision and pattern recognition, pp. 770–778.
- Ho, J., Jain, A., Abbeel, P., 2020. Denoising diffusion probabilistic models. *Advances in neural information processing systems* 33, 6840–6851.
- Hoopes, A., Mora, J.S., Dalca, A.V., Fischl, B., Hoffmann, M., 2022. Synthstrip: skull-stripping for any brain image. *NeuroImage* 260, 119474.
- Hou, X., Shen, L., Sun, K., Qiu, G., 2017. Deep feature consistent variational autoencoder, in: 2017 IEEE Winter Conference on Applications of Computer Vision (WACV), IEEE Computer Society, Los Alamitos, CA, USA. pp. 1133–1141.
- Ioffe, S., Szegedy, C., 2015. Batch normalization: Accelerating deep network training by reducing internal covariate shift, in: International conference on machine learning, pmlr. pp. 448–456.
- Isola, P., Zhu, J.Y., Zhou, T., Efros, A.A., 2017. Image-to-image translation with conditional adversarial networks, in: Proceedings of the IEEE conference on computer vision and pattern recognition, pp. 1125–1134.
- Jang, S.I., Lois, C., Thibault, E., Becker, J.A., Dong, Y., Normandin, M.D., Price, J.C., Johnson, K.A., Fakhri, G.E., Gong, K., 2023. Taupetgen: Text-conditional tau pet image synthesis based on latent diffusion models. arXiv preprint arXiv:2306.11984 .
- Javed, K., Din, N.U., Bae, S., Maharjan, R.S., Seo, D., Yi, J., 2019. Umgan: Generative adversarial network for image unmosaicing using perceptual loss, in: 2019 16th International Conference on Machine Vision Applications (MVA), IEEE. pp. 1–5.
- Johnson, J., Alahi, A., Fei-Fei, L., 2016. Perceptual losses for real-time style transfer and super-resolution, in: Computer Vision–ECCV 2016: 14th European Conference, Amsterdam, The Netherlands, October 11–14, 2016, Proceedings, Part II 14, Springer. pp. 694–711.
- Kingma, D.P., Ba, J., 2014. Adam: A method for stochastic optimization. arXiv preprint arXiv:1412.6980 .

- Knopman, D.S., Amieva, H., Petersen, R.C., Chételat, G., Holtzman, D.M., Hyman, B.T., Nixon, R.A., Jones, D.T., 2021. Alzheimer disease. *Nature reviews Disease primers* 7, 33.
- Krizhevsky, A., Sutskever, I., Hinton, G.E., 2012. Imagenet classification with deep convolutional neural networks. *Advances in neural information processing systems* 25.
- Leuzy, A., Chiotis, K., Lemoine, L., Gillberg, P.G., Almkvist, O., Rodriguez-Vieitez, E., Nordberg, A., 2019. Tau pet imaging in neurodegenerative tauopathies—still a challenge. *Molecular psychiatry* 24, 1112–1134.
- Liu, Y., Chen, H., Chen, Y., Yin, W., Shen, C., 2021. Generic perceptual loss for modeling structured output dependencies, in: *Proceedings of the IEEE/CVF Conference on Computer Vision and Pattern Recognition*, pp. 5424–5432.
- Loshchilov, I., Hutter, F., 2016. Sgdr: Stochastic gradient descent with warm restarts. *arXiv preprint arXiv:1608.03983* .
- Mattay, V.S., Fotenos, A.F., Ganley, C.J., Marzella, L., 2020. Brain tau imaging: Food and drug administration approval of 18f-flortaucipir injection. *Journal of Nuclear Medicine* 61, 1411–1412. URL: <https://jnm.snmjournals.org/content/61/10/1411>, doi:10.2967/jnumed.120.252254.
- Pan, S., Chang, C.W., Peng, J., Zhang, J., Qiu, R.L., Wang, T., Roper, J., Liu, T., Mao, H., Yang, X., 2023. Cycle-guided denoising diffusion probability model for 3d cross-modality mri synthesis. *arXiv preprint arXiv:2305.00042* .
- Petersen, G.C., Roytman, M., Chiang, G.C., Li, Y., Gordon, M.L., Franceschi, A.M., 2022. Overview of tau pet molecular imaging. *Current opinion in neurology* 35, 230–239.
- Qu, X., Wang, X., Wang, Z., Wang, L., Zhang, L., 2018. Perceptual-dualgan: perceptual losses for image to image translation with generative adversarial nets, in: *2018 International Joint Conference on Neural Networks (IJCNN)*, IEEE. pp. 1–8.
- Rasmussen, J., Langerman, H., 2019. Alzheimer’s disease—why we need early diagnosis. *Degenerative neurological and neuromuscular disease* , 123–130.
- Ronneberger, O., Fischer, P., Brox, T., 2015. U-net: Convolutional networks for biomedical image segmentation, in: *Medical image computing and computer-assisted intervention—MICCAI 2015: 18th international conference, Munich, Germany, October 5-9, 2015, proceedings, part III* 18, Springer. pp. 234–241.
- Shin, H.C., Ihsani, A., Xu, Z., Mandava, S., Sreenivas, S.T., Forster, C., Cha, J., Initiative, A.D.N., 2020. Gandalf: Generative adversarial networks with discriminator-adaptive loss fine-tuning for alzheimer’s disease diagnosis from mri, in: *Medical Image Computing and Computer Assisted Intervention—MICCAI 2020: 23rd International Conference, Lima, Peru, October 4–8, 2020, Proceedings, Part II* 23, Springer. pp. 688–697.

- Sikka, A., Peri, S.V., Bathula, D.R., 2018. Mri to fdg-pet: cross-modal synthesis using 3d u-net for multi-modal alzheimer’s classification, in: Simulation and Synthesis in Medical Imaging: Third International Workshop, SASHIMI 2018, Held in Conjunction with MICCAI 2018, Granada, Spain, September 16, 2018, Proceedings 3, Springer. pp. 80–89.
- Simonyan, K., Zisserman, A., 2015. Very deep convolutional networks for large-scale image recognition, in: 3rd International Conference on Learning Representations.
- Sled, J.G., Zijdenbos, A.P., Evans, A.C., 1998. A nonparametric method for automatic correction of intensity nonuniformity in mri data. *IEEE transactions on medical imaging* 17, 87–97.
- Smith, L.N., 2017. Cyclical learning rates for training neural networks, in: 2017 IEEE winter conference on applications of computer vision (WACV), IEEE. pp. 464–472.
- Srivastava, N., Hinton, G., Krizhevsky, A., Sutskever, I., Salakhutdinov, R., 2014. Dropout: a simple way to prevent neural networks from overfitting. *The journal of machine learning research* 15, 1929–1958.
- The General Hospital Corporation (MGH), 2023. Freesurfer. URL: <https://surfer.nmr.mgh.harvard.edu>. version 7.4.1.
- Ulyanov, D., Vedaldi, A., Lempitsky, V., 2016. Instance normalization: The missing ingredient for fast stylization. *arXiv preprint arXiv:1607.08022* .
- Vaquero, J.J., Kinahan, P., 2015. Positron emission tomography: current challenges and opportunities for technological advances in clinical and preclinical imaging systems. *Annual review of biomedical engineering* 17, 385–414.
- Wang, Z., Bovik, A.C., Sheikh, H.R., Simoncelli, E.P., 2004. Image quality assessment: from error visibility to structural similarity. *IEEE transactions on image processing* 13, 600–612.
- Xie, T., Cao, C., Cui, Z., Guo, Y., Wu, C., Wang, X., Li, Q., Hu, Z., Sun, T., Sang, Z., et al., 2023. Synthesizing pet images from high-field and ultra-high-field mr images using joint diffusion attention model. *arXiv preprint arXiv:2305.03901* .
- Yang, H., Sun, J., Carass, A., Zhao, C., Lee, J., Xu, Z., Prince, J., 2018. Unpaired brain mr-to-ct synthesis using a structure-constrained cycleGAN, in: Deep Learning in Medical Image Analysis and Multimodal Learning for Clinical Decision Support: 4th International Workshop, DLMIA 2018, and 8th International Workshop, ML-CDS 2018, Held in Conjunction with MICCAI 2018, Granada, Spain, September 20, 2018, Proceedings 4, Springer. pp. 174–182.
- Zhang, J., He, X., Qing, L., Gao, F., Wang, B., 2022. Bpgan: Brain pet synthesis from mri using generative adversarial network for multi-modal alzheimer’s disease diagnosis. *Computer Methods and Programs in Biomedicine* 217, 106676.

Zhu, J.Y., Park, T., Isola, P., Efros, A.A., 2017. Unpaired image-to-image translation using cycle-consistent adversarial networks, in: Proceedings of the IEEE international conference on computer vision, pp. 2223–2232.